Optics Letters

Ultra-compact silicon mode-order converters based on dielectric slots

Yaotian Zhao, Xuhan Guo,* Yong Zhang, Jinlong Xiang, Kangnian Wang, Hongwei Wang, and Yikai Su

State Key Laboratory of Advanced Optical Communication Systems and Networks Department of Electronic Engineering, Shanghai Jiao Tong University, Shanghai 200240, China
**Corresponding author: guoxuhan@sjtu.edu.cn*

Received 2 March 2020; revised 9 May 2020; accepted 28 May 2020; posted 29 May 2020 (Doc. ID 391748); published 1 July 2020

Ultra-compact mode-order converters with dielectric slots are demonstrated on a silicon-on-insulator platform. We propose a mode converter that converts the TE0 mode into the TE1 mode with an ultra-small footprint of only 0.8 × 1.2 μm². The measured insertion loss is less than 1.2 dB from 1520 nm to 1570 nm. To reduce the insertion loss, we further optimize the structure and design two mode converters that convert the TE0 mode into the TE1 mode and the TE2 mode with footprints of 0.88 × 2.3 μm² and 1.4 × 2.4 μm², respectively. Their measured insertion losses are both less than 0.5 dB. Additionally, the proposed devices are cascadable and scalable for high-order mode conversion.

https://doi.org/10.1364/OL.391748

Multimode manipulation in silicon photonics is one of the most promising technologies to accommodate the increasing demand for the communication capacity [1]. Lots of functional devices have been reported to realize a mode-division multiplexing (MDM) system, such as mode (de)multiplexers [2–4], multimode waveguide bends [5], multimode waveguide crossings [6], and reconfigurable multimode devices [7]. Mode converters that can transform a mode into another mode are widely explored among these key components. Different structures for mode converters have been reported, and three methods are mainly used to achieve mode conversions: phase matching [2,3], coherent scattering [4], and beam shaping [7,8]. However, there are still some challenges to handle the device footprints, operation bandwidth and fabrication tolerance simultaneously.

Recently, dielectric metasurface structures have emerged to design mode-order converters [9–18]. Based on those structures, mode converters can realize high-quality mode conversion with small footprints. For example, our previous designs show that the metasurfaces based on etched slots in silicon waveguides can realize mode conversion with good performances [18].

In this Letter, we propose ultra-compact silicon mode-order converters exploiting the fully etched dielectric slots. The etched dielectric slots can strongly manipulate the phase and amplitude of the guided modes simultaneously and convert them into the desired modes. The mode-order conversion from the TE0 mode into the TE1 mode can be realized within a length of only 1.2 μm employing the simply fully etched dielectric slot. By adjusting the shape of the slot, we can further reduce the insertion loss at the cost of relatively longer coupling length. As design examples, two mode-order converters are demonstrated with the coupling lengths of 2.3 μm and 2.4 μm respectively, and the measured insertion losses are both less than 0.5 dB. Besides, we analyze a two-stage mode-order converter for TE0-to-TE3 mode conversion to verify the cascadability and scalability of this type of mode-order converter based on dielectric slots.

The working principle of these devices is similar to that of the Mach–Zehnder interferometer (MZI)-based mode converters [7,8], which is called the beam shaping method. Taking the TE0-to-TE1 mode conversion as an example, two antiphase TE0-like modes can combine and produce a TE1 mode due to their similar mode profiles [19]. We demonstrate the working principle in detail with Fig. 1(a). The input TE0 mode is split into two beams with equal powers, and a phase shifter induces a phase difference of π between the two beams at the same time during the propagation. In the end, the two antiphase TE0 modes recombine and generate a TE1 mode.

Our proposed ultra-compact TE0-to-TE1 mode converter is schematically shown in Fig. 1(b), which is based on a regular silicon-on-insulator (SOI) substrate consisting of a thin silicon layer of 220 nm on top of a 3 μm buried oxide layer. The dielectric slot is fully etched in a silicon waveguide and filled with silica. The structure can be effectively regarded as a combination of a beam splitter and a taper phase shifter. The off-center silica slot is similar to a Y beam splitter and divides the light into two parts. The power splitting ratio can be controlled by adjusting the center of the slot (W_2 and W_3). Also, the taper structure is used as a phase shifter as the effective index changes with the width of the waveguide. Therefore, if the upper and lower waveguides have different widths as shown in Fig. 1(b), the propagation constants and phase velocities will also be different, which can generate a phase difference. By engineering the power splitting ratio and the phase difference, the two beams can have equal powers and a π phase difference. Then the two beams recombine to produce a TE1 mode.

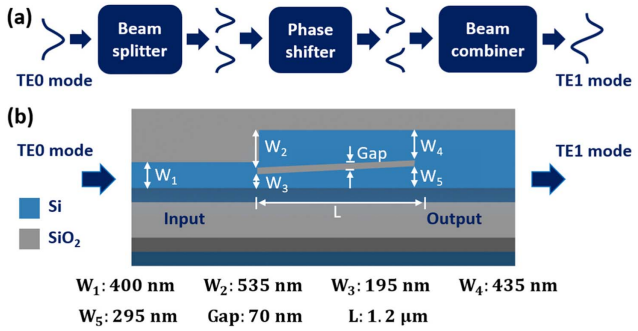

Fig. 1. (a) Schematic diagram of the beam shaping method. (b) Ultra-compact TE0-to-TE1 mode converter.

The coupled mode theory (CMT) together with the effective index method (EIM) is used to describe the mutual interaction between the propagation modes in the optical waveguide. We first obtain the electric field distribution of the eigenmodes in the waveguide from the EIM method. Assuming that the modes propagate along the z direction, the profile of the mth-order mode can be expressed as $\Psi_m(x, y)$ [14]. Each mode is orthogonal to the other modes and has unity power flux in the z-direction as follows [13]:

$$\iint \Psi_m^*(x, y)\Psi_n(x, y)\mathrm{d}x\mathrm{d}y = \frac{2\omega\mu}{|\beta_m|}\delta_{mn}, \tag{1}$$

where ω is the angular frequency, μ is the free space permeability, β_m is the propagation constant of the mth-order mode, and δ_{mn} is the Kronecker delta.

All the possible modes of the unperturbed waveguide form a complete orthonormal basis state, and the input field can be expanded using a superposition of these eigenmodes [20]:

$$E_{in}(x, y) = \sum_m \mathcal{A}_m(0)\Psi_m(x, y)e^{-j\beta_m z}, \tag{2}$$

where $\mathcal{A}_m(0)$ represents the complex transmission coefficient of the mth-order mode of the unperturbed waveguide at the beginning, and $\Psi_m(x, y)$ represents its electric field distribution. Likewise, the electric field in the propagating waveguide can be also expressed as a superposition of the eigenmodes as follows [14]:

$$E(x, y, z) = \sum_m \mathcal{A}_m(z)\Psi_m(x, y)e^{-j\beta_m z}. \tag{3}$$

The transmission coefficients $\mathcal{A}_m(z)$ are dependent on the propagation distance as a result of mode coupling, and the evolution of the coefficients $\mathcal{A}_m(z)$ can be driven by the CMT equations as follows [20]:

$$\frac{dA_m(z)}{dz} = -i\sum_n \kappa_{mn}(z)A_n(z)e^{-i(\beta_n-\beta_m)z}, \tag{4}$$

where κ_{mn} represents the coupling coefficients between the mth-order mode and the nth-order mode, which can be written as [20]

$$\kappa_{mn}(z) = \frac{\omega}{4}\iint \Psi_m^*(x, y)\Delta\varepsilon(x, y, z)\Psi_n(x, y)\mathrm{d}x\mathrm{d}y, \tag{5}$$

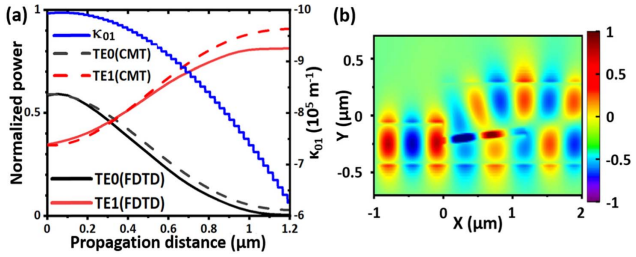

Fig. 2. (a) Coupling coefficient κ_{01} and the normalized power of each mode along the propagation calculated by the CMT equations or the 3D-FDTD method. (b) Simulated electric field (E_y) distribution.

where $\Delta\varepsilon(x, y, z)$ represents the dielectric perturbation in the silicon waveguide, which can be written as [14]

$$\Delta\varepsilon(x, y, z) = \begin{cases} \varepsilon_0(n_{\mathrm{Die}}^2 - n_{\mathrm{Si}}^2); & \text{if there is dielectric material,} \\ 0; & \text{otherwise.} \end{cases} \tag{6}$$

The ε_0 is the free space permittivity, n_{Si} and n_{Die} are the refractive index of the silicon and the dielectric material of silica respectively. Hence, the transmission coefficient of each mode $\mathcal{A}_m(z)$ can be calculated, and the power of each mode along the propagation can be obtaining in terms of the coupling coefficients as $|\mathcal{A}_m(z)|^2$ [20].

Based on the theoretical analysis above, we set the width of the input waveguide as 400 nm to support the TE0 mode and set the width of the output waveguide as 800 nm to support the TE0 and the TE1 modes [7]. The coupling length is set as 1.2 μm to be long enough to achieve the mode conversion completely. The width of the slot is set as 70 nm considering the feasible fabrication accuracy. Then we sweep the center of the slot (W_2 and W_3) and the taper widths (W_4 and W_5) to control the coupling coefficients, thus generating the TE1 mode. The optimized parameters are presented in Fig. 1(b). Figure 2(a) shows the coupling coefficient κ_{01} and the normalized power of each mode along the propagation. The conversion efficiency can be as large as 90% along the dielectric slot calculated by the CMT.

Then the three-dimensional finite-difference time-domain (3D-FDTD) method is implemented to verify the theoretical results of the device. In the simulation, we set the obtained parameters from the CMT method. The normalized power of each mode along the propagation is shown in Fig. 2(a). The results calculated by the 3D-FDTD method agree with that calculated by the CMT equations except that the conversion efficiency is slightly lower because we neglect the conversion loss when employing the CMT. Figure 2(b) shows the simulated electric field (Ey) distribution. It can be seen that the input TE0 mode is gradually converted into the TE1 mode, which agrees well with our previous analysis. Figure 3(a) shows the simulated transmission spectra of the mode converter; the insertion loss is less than 1.2 dB with crosstalk lower than −16.5 dB over a large bandwidth of 100 nm covering the whole C band.

It is worth mentioning that our devices have a relatively good fabrication tolerance in simulation. As shown in Fig. 3(b), when the width variation of the fully etched gap is as large as ±10 nm, the insertion loss is still less than 1.2 dB with the crosstalk lower than −20 dB at 1550 nm. However, the high fabrication resolution is still necessary since the width of the slot is only 70 nm.

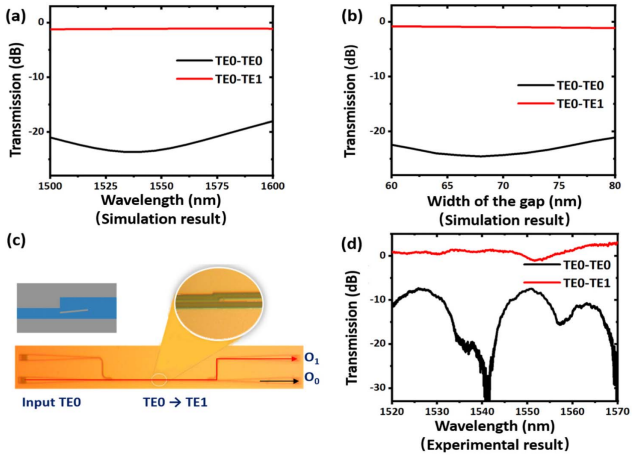

Fig. 3. Ultra-compact TE0-to-TE1 mode converter. (a) Simulated transmission spectra, (b) insertion loss and crosstalk with the gap width errors within ±10 nm, (c) optical microscope photo, and (d) measured transmission spectra.

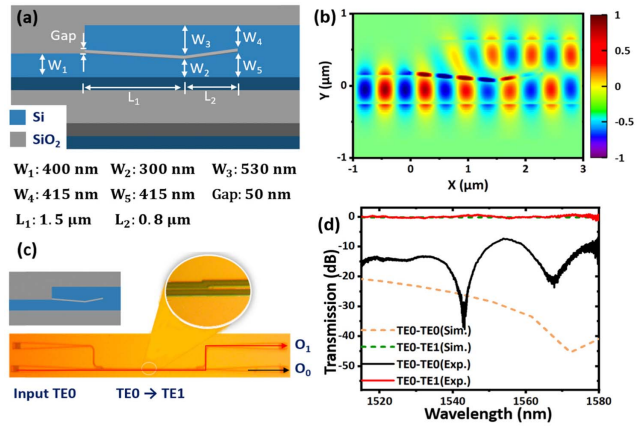

Fig. 4. Low loss TE0-to-TE1 mode converter. (a) Schematic diagram, (b) simulated electric field distribution, (c) optical microscope photo, and (d) simulation and experimental transmission spectra.

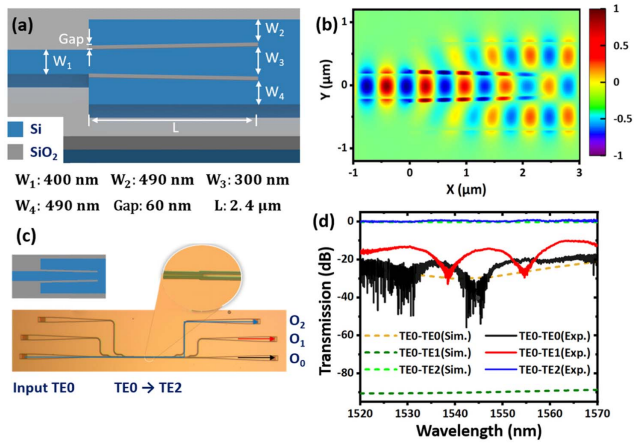

Fig. 5. Low loss TE0-to-TE2 mode converter. (a) Schematic diagram, (b) simulated electric field distribution, (c) optical microscope photo, and (d) simulation and experimental transmission spectra.

We fabricated the device on an SOI platform, and the structures were patterned employing e-beam lithography (EBL) and inductively coupled plasma (ICP) etching. An optical power meter and a tunable continuous wave (CW) laser were used to characterize the device. We also fabricated the grating couplers (GC) on the same wafer to couple light between the fibers and the silicon waveguides, and reference mode (de)multiplexers based on asymmetrical directional coupler (ADC) structures were cascaded to measure the insertion loss and crosstalk of our proposed mode-order converters [2]. Figure 3(c) shows the optical microscope photo of the fabricated structures. Unfortunately, we did not get a clear scanning electron microscope (SEM) photo due to the thick silica cladding. The input TE0 mode that has been converted into the TE1 mode by our device will then be coupled into the O_1 port. The unconverted TE0 mode will be coupled into the O_0 port as the crosstalk. Figure 3(d) depicts the measured transmission spectra of the device, which are normalized according to the reference GC and the reference mode (de)multiplexers fabricated on the same wafer, and the insertion loss is measured to be less than 1.2 dB with the crosstalk lower than −6.3 dB from 1520 nm to 1570 nm. Since the ADC-based mode (de)multiplexers are sensitive to the fabrication deviations, there is some discrepancy between the performances of the reference (de)multiplexers and the (de)multiplexers employed in our test device, especially over a large bandwidth (∼50 nm). Thus the measured loss of the device may show certain errors especially at the longer wavelengths, and the crosstalk of the device is not as good as the simulation results.

In addition to the mode converters that have been demonstrated above, we propose a practical method to reduce the insertion loss of the mode converter, though at the cost of relatively longer coupling length. Here, the low loss TE0-to-TE1 mode converter is demonstrated in Fig. 4(a). In our previous design, we observe a relatively high insertion loss. To solve this problem, we utilize the evanescent wave coupling to realize the function of a beam splitter. The simulated electric field (E_y) distribution calculated by the 3D-FDTD method is shown in Fig. 4(b). The optical microscope photo of the fabricated structures is shown in Fig. 4(c) as previous. Figure 4(d) shows the simulation and experimental transmission spectra of the device, which indicate that the insertion loss is less than 0.15 dB with crosstalk lower than −20 dB in the simulation, and the insertion loss is less than 0.5 dB with the crosstalk lower than −7 dB from 1520 nm to 1580 nm in the measurement.

Additionally, this design principle can be employed to realize higher-order mode conversions. As an example, a TE0-to-TE2 mode converter is schematically shown in Fig. 5(a). Likewise, Fig. 5(b) shows the simulated electric field (E_y) distribution in the 3D-FDTD simulation. Figure 5(c) shows the optical microscope photo of the fabricated structures. The cascaded mode (de)multiplexers will couple the output TE0, TE1, and TE2 modes into the O_0, O_1, and O_2 ports, respectively for the measurements. Figure 5(d) shows the simulation and experimental transmission spectra; the insertion loss is less than 0.22 dB with crosstalk lower than −18 dB in the simulation, and the insertion loss is less than 0.3 dB with the crosstalk lower than −9 dB from 1520 nm to 1570 nm in the measurement.

Furthermore, we can cascade the structure to realize high-order mode conversions if the desired mode cannot be directly obtained. Here we demonstrate a two-stage TE0-to-TE3 mode converter in simulation. Since two TE1-like modes in antiphase can combine and produce a TE3 mode, a similar structure

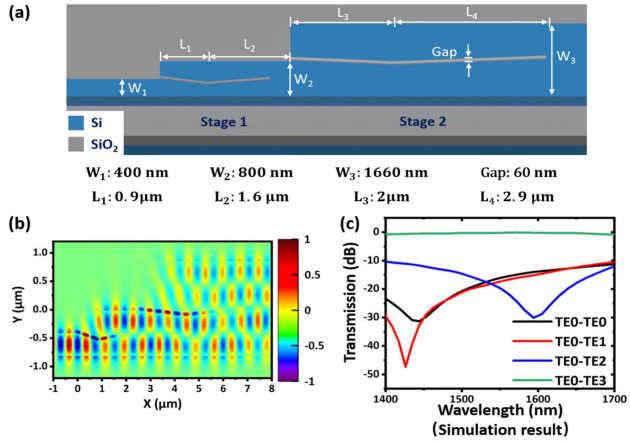

Fig. 6. Two-stage TE0-to-TE3 mode converter. (a) Schematic diagram, (b) simulated electric field (E_y) distribution, and (c) simulated transmission spectra.

Table 1. Comparison of Some Experimentally Demonstrated Mode Converters

References	Coupling Length (μm)	Insertion Loss (dB)	Crosstalk (dB)	Bandwidth (nm)	Device Function
[14]	2.635/2.27	2.1/1.37	−13.4/−12.6	45	TE0-to-TE1/TE2
[15]	5.75/6.736	<1	<−10	20	TE0-to-TE1/TE2
[16]	6.3	2	−12	43	TE0-to-TE1
[17]	4	<2.3	<−11.5	40	TE0-to-TE1&TM0-to-TM1
Our work	2.3/2.4	0.5/0.3	−7/−9	50	TE0-to-TE1/TE2
Our work	1.2	1.2	−6.3	50	TE0-to-TE1

could be cascaded after a TE0-to-TE1 mode converter to realize the TE0-to-TE3 mode conversion with a total length of only 7.4 μm as shown in Fig. 6(a). The simulated electric field (E_y) distribution in the 3D-FDTD method is shown in Fig. 6(b). In the first stage, the input TE0 mode is converted into the TE1 mode. In the second stage, the TE1 mode is gradually reshaped into two TE1-like modes in antiphase, which generates a TE3 mode. The simulated transmission spectra shown in Fig. 6(c) indicate that the insertion loss and crosstalk are less than 0.83 dB and −10 dB, respectively, over a broad bandwidth range of 300 nm. This method could be scaled to design high-order mode converters effectively.

Finally, we compare our designed structures with several reported mode converters based on metasurfaces that have been reported experimentally in Table 1. It shows that our work has greatly reduced the size of the mode converter, which is important for a high-density integration MDM system. The relatively high crosstalk may result from the presence of resonances in experiment due to the fabrication accuracy as analyzed before.

In summary, we proposed a concept for the ultra-compact mode converters with dielectric slots. The ultra-compact TE0-to-TE1 mode converter has been experimentally demonstrated with the footprint of only $0.8 \times 1.2\ \mu m^2$. To the best of our knowledge, this is the smallest until now. In addition, we adjust the structure to further reduce the insertion loss and design the TE0-to-TE1 and TE0-to-TE2 mode converters with short lengths (<2.4 μm), low insertion losses (<0.5 dB) and broad bandwidths (>50 nm). We also verify the scalability and cascadability of this concept with the two-stage TE0-to-TE3 mode converter in the simulation. We believe our proposed concept can offer an effective approach to design multimode silicon photonics devices which may further promote MDM optical systems for on-chip optical interconnections.

Funding. National Key Research and Development Program of China (2019YFB2203101); National Natural Science Foundation of China (61805137, 61835008); Natural Science Foundation of Shanghai (19ZR1475400); Shanghai Sailing Program (18YF1411900); Open Project Program of Wuhan National Laboratory for Optoelectronics (2018WNLOKF012).

Acknowledgment. We thank the Center for Advanced Electronic Materials and Devices (AEMD) of Shanghai Jiao Tong University (SJTU) for the support in device fabrications.

Disclosures. The authors declare no conflicts of interest.

REFERENCES

1. C. Li, D. Liu, and D. Dai, Nanophotonics **8**, 227 (2019).
2. Y. He, Y. Zhang, Q. Zhu, S. An, R. Cao, X. Guo, C. Qiu, and Y. Su, J. Lightwave Technol. **36**, 5746 (2018).
3. Y. Ding, J. Xu, F. Da Ros, B. Huang, H. Ou, and C. Peucheret, Opt. Express **21**, 10376 (2013).
4. Y. Li, C. Li, C. Li, B. Cheng, and C. Xue, Opt. Express **22**, 5781 (2014).
5. X. Jiang, H. Wu, and D. Dai, Opt. Express **26**, 17680 (2018).
6. W. Chang, L. Lu, X. Ren, L. Lu, M. Cheng, D. Liu, and M. Zhang, IEEE Photon. J. **10**, 4501008 (2018).
7. C. Sun, Y. Yu, G. Chen, and X. Zhang, Opt. Express **24**, 21722 (2016).
8. B. Lee and S. Shin, Opt. Lett. **28**, 1660 (2003).
9. L. Hao, R. Xiao, Y. Shi, P. Dai, Y. Zhao, S. Liu, J. Lu, and X. Chen, IEEE Photon. J. **11**, 6601210 (2019).
10. D. Ohana and U. Levy, Opt. Express **22**, 27617 (2014).
11. L. Liu, Y. Xu, L. Wen, Y. Dong, B. Zhang, and Y. Ni, Appl. Opt. **58**, 9075 (2019).
12. Z. Cheng, J. Wang, Z. Yang, L. Zhu, Y. Yang, Y. Huang, and X. Ren, Opt. Express **27**, 34434 (2019).
13. Y. Greenberg and A. Karabchevsky, Appl. Opt. **58**, F21 (2019).
14. B. E. Abu-Elmaaty, M. S. Sayed, R. K. Pokharel, and H. M. H. Shalaby, Appl. Opt. **58**, 1763 (2019).
15. H. Wang, Y. Zhang, Y. He, Q. Zhu, L. Sun, and Y. Su, Adv. Opt. Mater. **7**, 1801191 (2019).
16. L. H. Frandsen, Y. Elesin, L. F. Frellsen, M. Mitrovic, Y. Ding, O. Sigmund, and K. Yvind, Opt. Express **22**, 8525 (2014).
17. H. Jia, H. Chen, J. Yang, H. Xiao, W. Chen, and Y. Tian, Opt. Lett. **44**, 4179 (2019).
18. Y. Zhao, X. Guo, K. Wang, H. Wang, and Y. Su, *Asia Communications and Photonics Conference (ACPC)*, OSA Technical Digest (Optical Society of America, 2019), paper M3D.4.
19. D. Chen, X. Xiao, L. Wang, Y. Yu, W. Liu, and Q. Yang, Opt. Express **23**, 11152 (2015).
20. G. Lifante, *Integrated Photonics: Fundamentals* (Wiley, 2003), Chap. 4.